THE JOURNAL OF PHYSICAL CHEMISTRY C

Article

pubs.acs.org/JPCC

Redox Cycling in Nanopore-Confined Recessed Dual-Ring Electrode Arrays

Donghoon Han,[†] Lawrence P. Zaino, III,[‡] Kaiyu Fu,[‡] and Paul W. Bohn*[,†,‡]

[†]Department of Chemical and Biomolecular Engineering, University of Notre Dame, Notre Dame, Indiana 46556, United States

[‡]Department of Chemistry and Biochemistry, University of Notre Dame, Notre Dame, Indiana 46556, United States

Supporting Information

ABSTRACT: A redox cycling geometry based on an array of nanopore-confined recessed dual-ring electrodes (RDREs) has been devised to amplify electrochemical signals and enhance the sensitivity of electroanalytical measurements. The RDRE arrays were fabricated using layer-by-layer deposition followed by focused ion beam milling. A characteristic feature of the nanoscale dual-ring geometry is that electrochemical reactions occurring at the bottom-ring electrode can be tuned by modulating the potential at the top-ring electrode. Thus, the resulting device was operated in generator−collector mode by holding the top-ring electrodes at a constant potential and performing cyclic voltammetry by sweeping the bottom-ring potential in aqueous $Fe(CN)_6^{3-/4-}$. The enhanced (~23×) limiting current, achieved by cycling the redox couple between top- and bottom-ring electrodes with high collection efficiency, was compared with that obtained in the absence of self-induced redox cycling (SIRC). Measured shifts in $Fe(CN)_6^{3-/4-}$ concentration distributions were found to be in excellent agreement with finite-element simulations. The SIRC effect in the RDRE array was also characterized by electrochemical experiments before and after oxygen plasma treatment. The plasma-treated RDRE array exhibited a significant signal amplification, with the faradaic current being augmented by a factor of ~65 as a result of efficient redox cycling of electroactive species in the nanopores. The amplification factor of the devices was optimized by controlling the interpore distance, with larger pore density arrays exhibiting larger amplification factors.

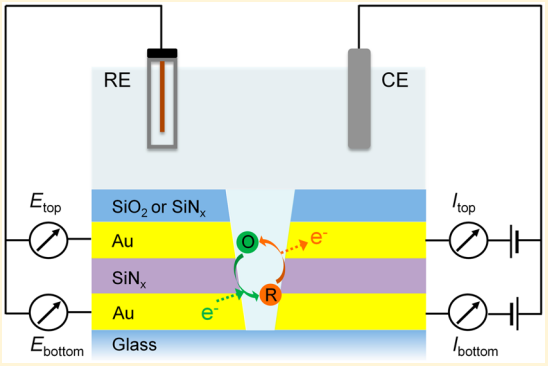

INTRODUCTION

Electrochemical redox cycling (RC) on the micro/nanoscale is a powerful tool for the amplification of faradaic currents in electroanalytical measurements, enhancing sensitivity through repetitive oxidation and reduction of the analyte. A typical approach to achieve repetitive redox reactions uses two closely spaced and individually addressable electrodes. Driven primarily by diffusion, the target molecules are transported between these electrodes when one electrode is biased to a reducing potential and the other electrode to an oxidizing potential.[1] When molecules diffuse from the cathode to the anode with each shuttling cycle, a feedback redox loop is established, which effectively amplifies the faradaic current. The RC current is proportional to the number of molecules contributing to the signal and can therefore be used for quantitative analyte detection[2] and can reach single-molecule detection under well-defined conditions.[3−5] RC not only can improve sensitivity[6,7] but also is useful for determining diffusion coefficients of redox species[8,9] and monitoring the lifetime of electrogenerated intermediates.[10,11]

RC can be enhanced by geometric configurations that allow two electrically addressable metal substrates to be positioned very close, that is, nanometer distances, to one another. For example, a probe-based configuration is employed in scanning electrochemical microscopy (SECM), which allows local electrochemical interface reactions to be resolved and imaged.[12] SECM has been used in a variety of applications ranging from topographic and reactivity studies on solid-state surfaces to the electrochemical imaging of living cells.[13] Other techniques aim to implement RC for electrochemical detection in lab-on-a-chip devices.[14] The advances of micro- and nanofabrication techniques during the last few decades have greatly improved the efficiency of lab-on-a-chip RC devices, and there have been a number of RC systems reported, for example, interdigitated array (IDA) electrodes,[15−18] twin-electrode thin-layer cell,[19,20] rotating ring-disc electrodes,[21,22] and a micromachined wall-jet ring-disc electrode.[23]

Pore-based structures supporting dual annular band electrodes constitute a separate and especially powerful class of RC devices because the electrodes can be positioned with a separation of tens to hundreds of nanometers from each other, thus facilitating very efficient diffusive transport.[24−32] Typically,

Special Issue: Richard P. Van Duyne Festschrift

Received: February 5, 2016
Revised: May 17, 2016
Published: May 18, 2016

DOI: 10.1021/acs.jpcc.6b01287
J. Phys. Chem. C 2016, 120, 20634−20641

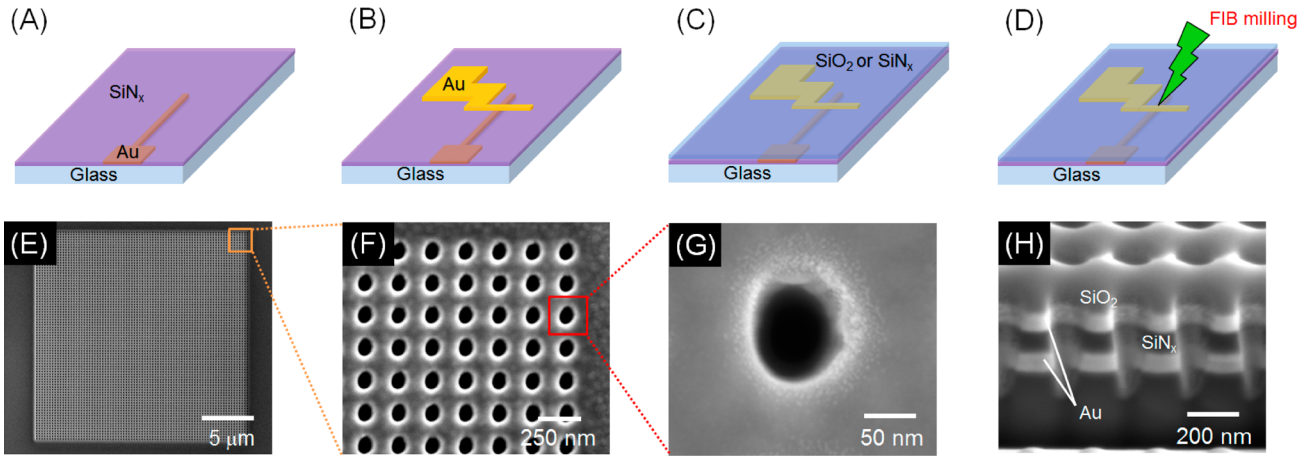

Figure 1. (A–D) Schematic illustration of the fabrication process for the RDRE array. (A) Bottom electrode is patterned with photolithography and Au is deposited by electron beam evaporation. Then, after metal lift-off, SiN_x is deposited by PECVD as an insulating layer. (B) Top electrode is patterned and deposited in a similar manner. (C) SiO_2 or SiN_x is deposited as a passivation layer. (D) Nanopores are patterned by FIB milling. (E–H) Scanning electron micrographs of a RDRE array at different magnifications and perspectives. (E) Top-down view of the entire 20 μm × 20 μm RDRE array. (F) Top-down view of a 7 × 7 subset of the same array. (G) Top-down view of a single nanopore and (H) cross-sectional SEM image of the nanopores taken at 52° tilt.

in pore-based RC devices, the working electrodes are stacked in vertical layers in a metal–insulator–metal (MIM) stack. Redox-active molecules gain access to the bottom electrode by transport down the axis of the nanopore past the top electrode and the insulator. Then, to enable RC inside the pores, the top and bottom electrodes are individually biased to electrochemical potentials below and above the redox potential of the analyte. Previously, this design has been implemented on the submicrometer length scale in RC structures with pore diameters of 500 nm, electrode separations of 200 nm, and interpore spacings of ~500 nm.[26] Surprisingly, the interpore spacing is an important design parameter, as molecules not collected at the top electrode of one pore may diffuse to a neighboring pore and be recaptured there.

Recently, we developed a robust procedure for the fabrication of recessed ring-disk electrode arrays with submicrometer size and spacing[30] and demonstrated their utility for RC in a variety of applications, including selective electrochemical detection,[31] ion accumulation-based signal amplification,[32] and self-induced redox cycling (SIRC) coupled to fluorescence sensing.[33] Because of their dimensions, nanopore sensors can further be used to detect selective binding to functionalized pore walls,[28] the RC effect being used to read out the behavior of a reporter whose mobility is reduced by the analytical target, such as an oligonucleotide. Moreover, enzymes can be attached to the pore walls and locally convert substrates to electroactive products.[34] Additionally nanopore-based sensors are based on a modular layout, in which the sensor output can be regarded as the sum of multiple single-pore elements. Because each of these elements is strongly coupled to the reservoir, short fluctuations in the analyte concentration can be detected. Also, the sensor area can be scaled without loss of structural integrity.

Nanoelectrode arrays are typically fabricated with top-down approaches, for example, using hybrid approaches, such as optical lithography,[35,36] colloidal lithography,[30,37] focused ion beam (FIB) milling,[38,39] and electron beam lithography to define nanostructures, as well as interconnected metallization and passivation layers.[40,41] Among the hybrid lithography approaches, FIB milling method receives particular attention because it is a serial direct-write technique capable of deep anisotropic etching that greatly aids the direct production of electrodes and arrays. Arrigan and coworkers[38] provided an early example of FIB-based nanoelectrodes, in which they fabricated single and ordered arrays of recessed nanopore electrodes. These devices were constructed on Si/SiO_2 substrates bearing photolithographically defined Pt microscale electrodes, followed by deposition of a ~500 nm thick insulating layer of SiN_x over the Pt electrodes. FIB milling was also utilized by Rauf et al.,[39] to produce discrete 3D Pt electrode arrays. Submicrometer pores were milled through an insulting layer to reveal Au electrodes, onto which Pt was subsequently electrodeposited. This drill-and-fill approach yielded 3D Pt nanoelectrode arrays, with the nanoelectrode protruding from the insulator substrate, rather than being inlaid or recessed.

Here we report a robust and reliable method for the fabrication of high areal density (up to 1.6×10^9 cm^{-2}) recessed dual-ring electrode (RDRE) arrays with electrode size, interelectrode separation, and interpore spacing all controlled on the nanometer length scale. The use of dual-ring arrays, instead of ring-disk arrays, facilitates spectroelectrochemical experiments because it allows optical access to RC of fluorigenic redox species. Arrays with varying pore density were fabricated and characterized by cyclic voltammetry (CV) employing the bottom ring and top ring as generator and collector electrodes, with the bottom generator electrode being swept and the top collector electrode being held at a constant potential. The SIRC effect was characterized by performing cyclic voltammetry at a recessed single-ring electrode as working electrode of equivalent area and comparing that to the performance of the RDRE array. Finite element simulations were performed and compared with experimental results to understand the influence of collector potential on reactions at the generator. Voltammetric responses to electroactive species were investigated before and after O_2-plasma treatment on the top dielectric layers to further confirm participation of SIRC at the RDRE array. Finally, the signal generation behavior of the RDRE devices was characterized as a function of interpore

DOI: 10.1021/acs.jpcc.6b01287
J. Phys. Chem. C 2016, 120, 20634–20641

separation, and the analytical performance of the RDRE array was found to depend sensitively on pore density.

EXPERIMENTAL SECTION

Chemicals and Materials. Potassium ferricyanide ($K_3Fe(CN)_6$), potassium chloride, sulfuric acid (95%), hydrogen peroxide (30%), acetone, and Au etchant ($KI-I_2$ solution) were obtained from Sigma-Aldrich. Photoresist (PR) AZ5214E (AZ Electronic Materials) and polydimethylsiloxane (PDMS) (Dow Corning) were used according to the manufacturers' specifications. Solutions for electrochemical measurements, consisting of 2.0 M KCl and 1 or 5 mM $K_3Fe(CN)_6$, were prepared using deionized (DI) water generated from a milli-Q Gradient water purification system (Millipore). All reagents were used as received without further purification.

Device Fabrication. The RDRE arrays were fabricated using a combination of standard photolithography, layer-by-layer deposition, and FIB milling. The fabrication strategy is illustrated schematically in Figure 1A–D. A glass coverslip was cleaned in piranha solution (3:1 sulfuric acid (95%)/hydrogen peroxide (30%); *Caution! Strong oxidizer. Use with extreme care.*), rinsed with DI water, and dried at 110 °C. The cleaned glass coverslip was patterned by photolithography using AZ5214E PR to define a bottom electrode with a width of 100 μm. A 100 nm thick Au film was deposited by electron-beam evaporation (UNIVEX 450B, Oerlikon) using 10 nm Ti as an adhesion layer on the patterned glass coverslip. Then, an acetone lift-off was used to remove the photoresist. A 100 nm thick SiN_x layer was then deposited on sample by plasma-enhanced chemical vapor deposition (PECVD 790, Plasma-Therm) (Figure 1A). Afterward, using the same lithographic method, the top Au electrode was deposited to overlap the bottom electrode in a perpendicular orientation, producing an intersection area of ca. 200 μm × 200 μm containing two Au layers separated by a SiN_x layer (Figure 1B). Next, an additional 100 nm thick SiO_2 layer was deposited after the removal of the photoresist covering the entire substrate (Figure 1C). A dual-source FIB instrument (Helios Nanolab 600, FEI Corp.) was used for milling and characterization. RDRE arrays were patterned in a 20 μm × 20 μm square array with lattice constants of 250 nm, 500 nm, or 1 μm (Figure 1D). FIB milling was performed at 30 kV acceleration, 0.28 nA ion aperture, and 0.1 μs dwell time to produce the RDRE array. Immediately after milling the device, an ohmic background current was observable. Figure S1 shows the current resulting from a small bias (10 mV) between the top and bottom electrode in a dry device immediately after fabrication (black line). This is presumably caused by a combination of redeposition of partially etched Au along the nanopore walls and implanted Ga^+, resulting in an electrical short between the two electrodes. This conducting layer was removed by immersing the device in dilute Au etchant solution for 5 min. After cleaning the device with DI water, the top and bottom electrodes were well-insulated, as indicated by the red line in Figure S1.

Modeling and Calculations. Modeling calculations were performed using finite element simulation software (COMSOL Multiphysics 5.0). The electrochemical system treated here is a simple outer-sphere heterogeneous electron-transfer reaction at the electrodes, $O + ne^- \rightarrow R$, where n is the number of electrons transferred. An RDRE array of 20 nanopores was simulated in a 2D geometry, consisting of recessed bottom-ring electrodes, a 100 nm insulating layer, recessed top-ring electrodes, and a 100 nm top insulator layer. The geometry is based on scanning electron micrographs (SEMs) of FIB cross sections. The domain above the pores was drawn sufficiently large (w = 1000 μm, h = 1000 μm) to avoid interference from boundaries, and the mesh was refined both within the nanopores and in the region just above the pores to provide sufficient resolution. For the case of high overpotential applied to the electrodes, constant-concentration boundary conditions were applied based on the assumption of complete oxidation or complete reduction on the electrode surfaces. Steady-state operation of the device was characterized by assuming that the diffusion coefficients of the reduced and oxidized forms are the same,[42] leading to the result that the sum of oxidized (C_O) and reduced (C_R) forms is constant over the diffusion space and is equal to the sum of the bulk concentration (C_{bulk}).[43] Details of the simulations are given in the Supporting Information.

Electrochemical Measurements. Cyclic voltammetry (CV) experiments were performed with a CH Instruments electrochemical analyzer (Model 842C) using a Pt wire and Ag/AgCl (RE-5B, BASi) as auxiliary and reference electrodes, respectively. The nanopore-confined top and bottom electrodes operate as separate working electrodes. All potentials are reported versus Ag/AgCl reference at 300 K. Both the reference electrode and auxiliary electrode were immersed in a 100 μL PDMS reservoir in direct fluid contact with the RDRE array. In all CV measurements, the potential of the bottom electrodes was swept, and the top electrodes were held at a constant potential (GC mode) or disconnected (non-GC mode).

RESULTS AND DISCUSSION

Fabrication and Structural Characterization. RDRE arrays with variable interpore spacings (250 nm, 500 nm, or 1 μm) were fabricated to form square arrays of annular insulator–electrode–insulator–electrode nanopore stacks, in which each electrode layer is individually addressable; that is, the electrodes of the same layer in each nanopore are always at the same potential. Figure 1A–D illustrates the fabrication process using photolithography, layer-by-layer deposition, and FIB milling to produce nanopore RDRE arrays. This simple direct-write approach enables direct formation of highly precise nanopore electrodes, but FIB direct writing produces pores with conical frustum shapes rather than the cylindrical shapes obtained using electron beam[40,41] or nanosphere lithography.[30,37]

Figure 1E shows an SEM image of the entire array with an interpore distance of 250 nm, while Figure 1F–G shows SEM images of the same array at different levels of magnification. Figure 1H shows a cross-section of the typical pores produced by FIB milling.[44] The overetched region below the Au/glass interface typically decreases with pore diameter, and well-controlled milling processes yield pores overetched by <100 nm. From bottom to top, the cross-section image in Figure 1H shows the bottom Au electrode (bright), silicon nitride (dark gray), the top Au electrode (bright), and silicon dioxide (gray). The nanopores exhibit a conical shape with a slightly larger aperture at the top electrode than at the bottom electrode. The typical diameter of the top of the pore (d_{top}) is ~100–120 nm, while the bottom diameter (d_{bottom}) is ~60–80 nm.

Current Amplification by RDRE Array. Figure 2 shows the cyclic voltammetry of 5 mM $K_3Fe(CN)_6$ in 2 M aqueous KCl supporting electrolyte obtained from a RDRE array with an interpore distance of 250 nm. The cyclic voltammogram (CV) in Figure 2A was obtained by sweeping the potential, E_b, of the bottom working electrode, WE_b, while the top working

DOI: 10.1021/acs.jpcc.6b01287
J. Phys. Chem. C 2016, 120, 20634–20641

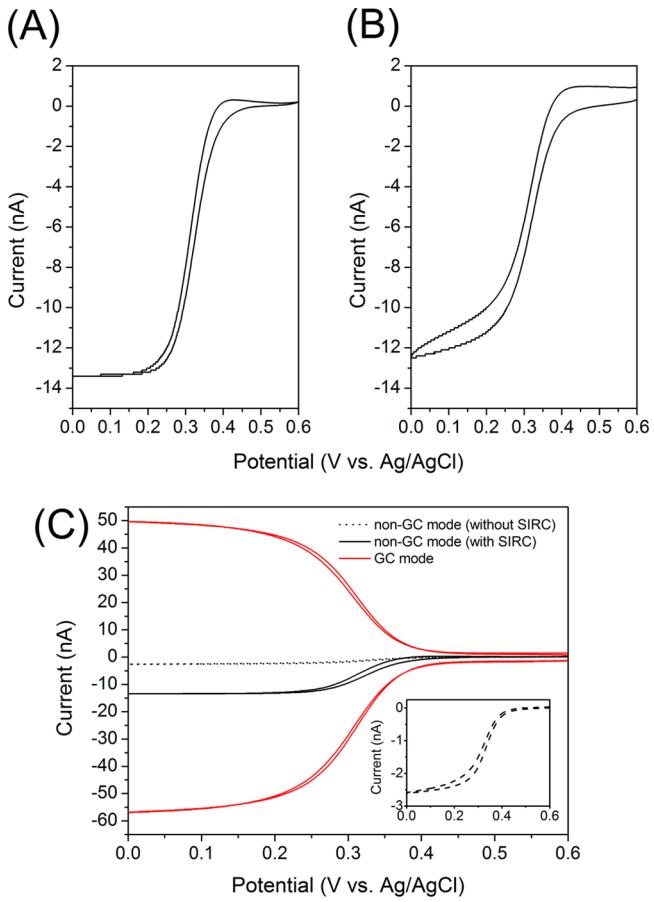

Figure 2. Cyclic voltammetry of 5 mM $Fe(CN)_6^{3-}$ in 2 M aqueous KCl (scan rate 50 mV/s) on an RDRE array with interpore distance of 250 nm. (A) Potential of the bottom electrode (E_b) was swept while the potential of top electrode (E_t) was left floating. (B) E_t was swept while E_b was left floating. (C) Cyclic voltammograms of 5 mM $Fe(CN)_6^{3-}$ in 2 M aqueous KCl (scan rate 50 mV/s) on the RDRE array (black and red line) and on a recessed single-ring electrode of the same area (Inset, magnified). E_b was swept, while E_t was floating (non-GC mode, black line) or held at +0.6 V (GC mode, red line). In GC mode current was measured at both the bottom (negative current) and top (positive current) working electrodes, although only the potential E_b was swept.

electrode, WE_t, was floating (disconnected). The current at WE_b reached a steady-state diffusion-limited plateau, $i_{lim} \approx -13$ nA, at large overpotentials. Figure 2B shows a CV obtained by sweeping the potential, E_t, of WE_t, while the bottom electrode was disconnected. The CVs shown in Figure 2A,B are very similar, reflecting the nearly identical electrochemical behavior of the two working electrodes. WE_t and WE_b have the same thickness and are separated by only 100 nm, so the difference in their surface areas, due to the conical nanopore shape, is <20%, and the small differences in shape and i_{lim} likely result from small differences in mass transport to WE_b relative to WE_t. On the contrary, the CV (red line) in Figure 2C was acquired by scanning E_b, while E_t was fixed at +0.6 V versus Ag/AgCl (GC mode). The current in GC mode (red line, $i_{lim} \approx -57$ nA) is ca. 4.4 times higher than that in the non-GC mode (black line in Figure 2C). This current amplification is attributed to RC of the electroactive species between generator and collector electrodes. The RC effect depends strongly on the efficiency, Φ_t, with which the top working electrode, WE_t, collects species generated at the generator.[16] Under the conditions of Figure 2C, the collection efficiency of the top electrode, Φ_t, is

$$\Phi_t = \frac{i_{t,la}}{i_{b,lc}} \quad (1)$$

where $i_{t,la}$ and $i_{b,lc}$ are the anodic and cathodic limiting currents at WE_t and WE_b, respectively. Using eq 1, Φ_t = 0.89 was obtained from the results shown in Figure 2C.

In general RC measurements, two electrodes are held at potentials negative and positive of the redox potential to initiate and sustain electrochemical RC. Interestingly, SIRC can be observed when a potential-controlled electrode is placed adjacent to a nearby unbiased (floating) electrode.[45,46] In this situation, depletion of redox species at the working electrode produces a location-dependent concentration polarization relative to the adjacent electrode. These local concentration differences can be sufficient to drive oxidation and reduction reactions at the floating electrode. To characterize the SIRC effect of the RDRE, we acquired CVs from a recessed single-ring electrode array of the same size, that is, an array with the same geometry as the RDRE array but without top insulator and Au layers, for comparison. With this system, no SIRC was expected from CVs obtained in non-GC mode (inset, Figure 2C), and thus only a small limiting current ($i_{lim} \approx -2.5$ nA) was observed as a result of faradaic reaction, which was limited by mass transfer from the bulk solution. The current in GC mode obtained from the RDRE array (red line in Figure 2C) is ca. 23 times higher than that in the non-GC mode in the absence of the SIRC effect.

Effect of WE_t Potential. In preliminary experiments, the collector (top) electrode was held at an anodic potential to oxidize the $Fe(CN)_6^{4-}$, generated at the bottom electrode, back to $Fe(CN)_6^{3-}$, which diffuses to the bottom electrode for electrochemical regeneration. This triggers a feedback loop that enables RC, which is the principal goal of constructing these nanoscale RDRE arrays. Although it is common with GC mode measurements for the collector to regenerate the initial species, modulation of the top electrodes to potentials closer to the generator electrode can also be useful in discriminating different electroactive species[6,29] or mitigating interferences.[29,47] Accordingly, we investigated the influence of E_t on the resulting voltammetric response and computed concentration profiles.

Figure 3A shows CVs obtained for a RDRE array with interpore distance of 250 nm in 5 mM $K_3Fe(CN)_6$ with 2 M KCl supporting electrolyte. The voltammograms were obtained by scanning E_b, while E_t was held constant at +0.6 V (oxidizing potential) or 0 V (reducing potential). In all cases the current through the bottom electrode (solid line) was essentially the inverse of that through the top electrode (dashed line) due to RC. When the fixed potential of the top electrode is +0.6 V (black curves Figure 3A), the anodic current is collected at WE_t, and the cathodic current is collected at WE_b in the reducing region of E_b, ca. 0 to +0.3 V versus Ag/AgCl. Conversely, when the fixed potential of WE_t is set at the cathodic value of 0 V (blue curves in Figure 3A), the cathodic current is collected at the WE_t, and the anodic current is collected at WE_b in the oxidizing region of E_b, ca. + 0.3 to +0.6 V versus Ag/AgCl.

Only cathodic current is observed at WE_b when WE_t is held at the oxidizing potential of +0.6 V. This is further confirmed by the simulated concentration profile of $Fe(CN)_6^{3-}$ in the nanopores shown in Figure 3B. Only oxidized species are

DOI: 10.1021/acs.jpcc.6b01287
J. Phys. Chem. C 2016, 120, 20634−20641

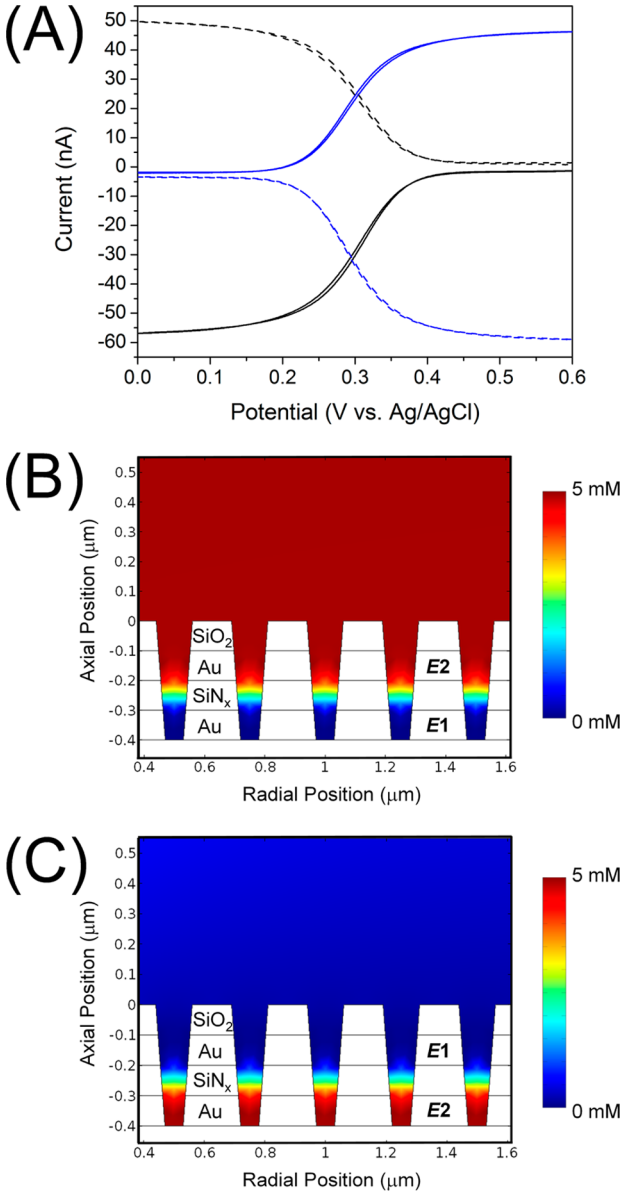

Figure 3. (A) Dependence of voltammetric response on E_t. Data acquired from 5 mM $Fe(CN)_6^{3-}$ in 2 M aqueous KCl (scan rate 50 mV/s) on a RDRE array with interpore distance of 250 nm. E_t was held at +0.6 V (black) and 0 V (blue); current at WE_b (solid) and WE_t (dashed). (B,C) Concentration profiles of $Fe(CN)_6^{3-}$ in adjacent pores by applying reducing (*E*1) and oxidizing (*E*2) potentials at the electrodes. The color scale shows the concentration distribution of redox species for the device (red: fully oxidized, blue: fully reduced).

available to WE_b because WE_t rapidly oxidizes all $Fe(CN)_6^{4-}$ generated at WE_b. When WE_t is held at 0 V, current at WE_b is predominantly anodic because $Fe(CN)_6^{3-}$ is depleted at WE_t, as seen in Figure 3C.

As illustrated in Figure 3A, the collection efficiency of WE_b, Φ_b, can be estimated by holding WE_t at 0 V while scanning the potential of WE_b. In this case, $Fe(CN)_6^{4-}$ generated at the WE_t is collected by and oxidized at WE_b, with Φ_b then being determined by

$$\Phi_b = \frac{i_{b,la}}{i_{t,lc}} \quad (2)$$

where $i_{b,la}$ and $i_{t,lc}$ are the anodic and cathodic limiting currents at WE_b and WE_t, respectively. $\Phi_b = 0.87$ was obtained from the results (blue curves) in Figure 3A. Using the method proposed by Tabei et al.,[16] the number of RC events, N_{RC}, is directly related to the current amplification and is given by

$$N_{RC} = \frac{1}{1 - \Phi_t\Phi_b} \quad (3)$$

For the RDRE array described, $\Phi_t = 0.89$ and $\Phi_b = 0.87$, yielding $N_{RC} = 4.4$, consistent with $AF_{SIRC} = 4.4$, defined as the ratio between the cathodic limiting currents obtained in GC mode and non-GC mode from the RDRE array in the presence of SIRC.

Controlling SIRC by O_2 Plasma Treatment. The SIRC effect has been observed previously on IDA electrodes and planar-recessed disk electrodes.[33,45,46] In these RDRE arrays the extent of SIRC can be controlled through the exposure of the top Au surface to the bulk solution by providing access to the Au through process-induced defects in the top SiO_2 film. These defects were introduced here by exposing the as-prepared structure to an O_2 plasma prior to electrochemical characterization. Figure 4 shows the CVs of an RDRE array with

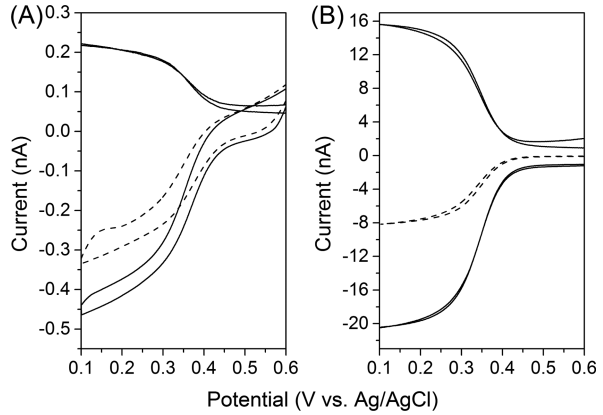

Figure 4. Cyclic voltammetry of 5 mM $Fe(CN)_6^{3-}$ in 2 M aqueous KCl (scan rate 50 mV/s) (A) before and (B) after O_2 plasma treatment of the RDRE array with interpore distance of 500 nm for 20 min. The potential at WE_b was swept, while WE_t was either disconnected (dashed line, non-GC mode) or held at +0.6 V (solid line, GC mode).

interpore distance of 500 nm, both before and after the O_2 plasma treatment. Before O_2 plasma treatment, a small electrochemical response, $i_{lim} \approx -300$ and -450 pA, stemming from the $Fe(CN)_6^{3-/4-}$ redox couple in both non-GC mode and GC mode is observed (Figure 4A). The amplification factor in these measurements is ca. 1.5 and the collection efficiency of the top electrode, Φ_t, is ~0.5. The capacitive contribution to the current at WE_b is more significant than at WE_t (solid line in Figure 4A). This is attributed primarily to imperfect insulation between WE_t and WE_b, which leads to charge leakage and the small charging current observed at WE_t. After O_2 plasma treatment, the CV in non-GC mode is sigmoidal and steady-state (dashed line Figure 4B). In GC mode (Figure 4B, solid line), steady-state waves are observed similar to those obtained in the presence of SIRC, cf. Figure 2C. This difference in voltammetric response between non-GC mode operation in Figure 4A,B is attributed to the SIRC effect mediated by the redox reactions accessed by the mechanical defects introduced

DOI: 10.1021/acs.jpcc.6b01287
J. Phys. Chem. C 2016, 120, 20634−20641

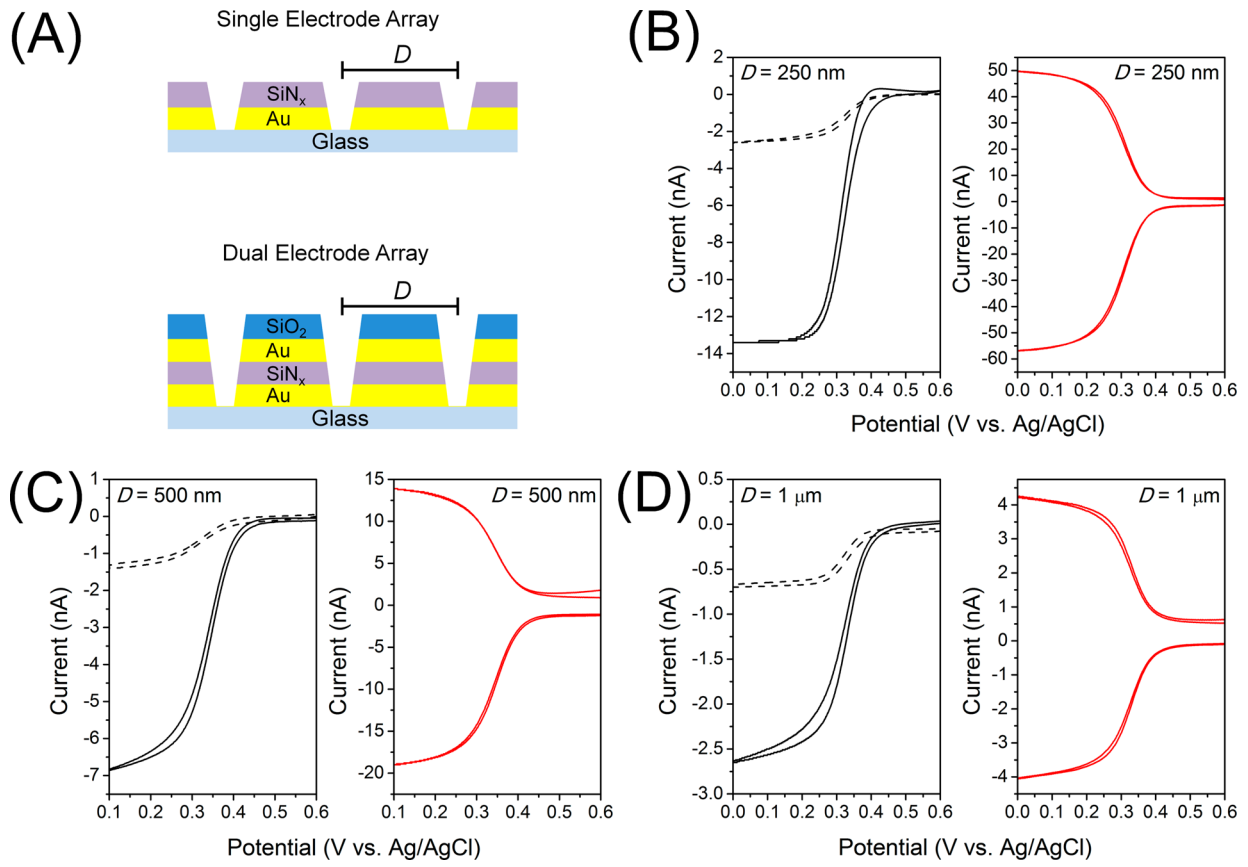

Figure 5. (A) Schematic illustration of recessed single/dual-ring electrode arrays. (B–D) Cyclic voltammetry as a function of interpore spacing at (B) 250 nm, (C) 500 nm, and (D) 1 μm. Left: voltammetric responses of the RDRE array in non-GC mode operation in the absence (dashed lines) and presence (solid lines) of SIRC in 5 mM $Fe(CN)_6^{3-}$ containing 2 M aqueous KCl supporting electrolyte (scan rate 50 mV/s). Right: voltammetric responses of the RDRE array at WE_t and WE_b in GC mode in 5 mM $Fe(CN)_6^{3-}$ containing 2 M aqueous KCl supporting electrolyte at 50 mV/s.

by O_2 plasma treatment. The current in GC mode at WE_b is amplified by 2.5 times relative to that in non-GC mode, and the collection efficiency at WE_t is $\Phi_t \approx 0.8$. Thus, a processing-induced amplification factor can be defined for this experiment as the ratio between the cathodic current in GC mode after exposure of the RDRE array to O_2 plasma, ca. 20.5 nA in Figure 4B, and the cathodic current in non-GC mode from the same array prior to O_2 exposure, ca. 0.3 nA in Figure 4A. This ratio between the current in GC mode (including any residual SIRC effect) and the current in non-GC mode without SIRC is ~ 65.

Effect of RDRE Array Geometry. The pore density of the devices, determined by the interpore distance of the RDRE array, is a major determinant of device performance. To characterize this relationship, we fabricated RDRE arrays with varying electrode density by patterning different interpore distances, D = 250 nm, 500 nm, and 1 μm, as shown in Figure 5A. All designs were 20 μm × 20 μm square arrays, yielding 6561, 1681, and 441 pores for the RDRE arrays with interpore spacings of 250 nm, 500 nm, and 1 μm, respectively. The GC mode CVs obtained from RDRE arrays with different interpore spacings (red lines in Figure 5B–D) show limiting currents, i_{lim} = −57, −19, and −4 nA on arrays with interpore distances of D = 250 nm, 500 nm, and 1 μm, respectively. These limiting currents are proportional to the number of nanopores in the array, reflecting the ca. 16:4:1 ratio determined by the nanopore density.

The geometric effect on the performance of RDRE arrays was obtained from the CVs at the three different pore densities with E_t floating, non-GC mode (solid lines in Figure 5B–D) and with E_t held at +0.6 V, GC mode (red lines in Figure 5B–D). To assess the SIRC effect, we investigated recessed single-ring electrode arrays (top structure in Figure 5A), and the CVs of three such arrays with different interpore spacings (250 nm, 500 nm, 1 μm) were also acquired (dashed lines in Figure 5B–D). The CVs in non-GC mode of arrays with different pore densities (dashed and solid lines in Figure 5B–D) are approximately sigmoidal and yield modest limiting currents, whereas the voltammetric responses of the same arrays in GC mode (red lines in Figure 5B–D) exhibit behavior typical of generator–collector systems, that is, sigmoidal current response, nearly symmetric responses between WE_b and WE_t, and strong amplification. The dependence of signal amplification on pore density, as summarized in Table 1, shows a strong correlation between pore density and AF_{SIRC}. In addition, a maximum amplification factor (AF_{max}) can be defined as the ratio between the cathodic current in GC mode from the RDRE array and the cathodic current in non-GC mode from a recessed single-ring electrode array at the same pore density. The largest maximum amplification factor, AF_{max}, is also observed at high-density, D = 250 nm, arrays and falls at medium, D = 500 nm, and low, D = 1 μm, densities. This behavior indicates that the pore density of dual-ring electrode arrays makes a substantial contribution to increasing signal

DOI: 10.1021/acs.jpcc.6b01287
J. Phys. Chem. C 2016, 120, 20634–20641

Table 1. Amplification Factors for RDRE Arrays with Different Pore Densities

interpore distance (D)	AF_{SIRC} [a]	AF_{max} [b]
250 nm (high-density)	4.4	22.8
500 nm (medium-density)	2.8	13.6
1 μm (low-density)	1.5	5.7

[a] AF_{SIRC} is defined as the ratio between the cathodic current in GC mode and non-GC mode from the RDRE array. [b] AF_{max} is defined as the ratio between the cathodic current in GC mode from the RDRE array and the cathodic current in non-GC mode from the recessed single-ring electrode array at the same pore density.

amplification, most reasonably due to considerable diffusion zone overlap producing a secondary trapping effect, in which a molecule escaping one nanopore can be captured and reacted by the annular WE_t at a neighboring nanopore.

CONCLUSIONS

We have demonstrated a new strategy for signal amplification based on geometrically efficient RC in a RDRE array containing two closely spaced working electrode layers separated by a thin insulator film. The proposed RDRE array was fabricated and shown to work as a generator−collector system with high collection efficiency. When operated in the GC mode, dramatic improvements in electrochemical performance can be realized relative to non-GC mode operation without SIRC effect. Both electrochemical experiments and finite-element simulation show that modulation of the potential at the top-ring electrodes can control the reaction at the bottom-ring electrodes. In addition, SIRC with current amplification up to 65-fold was observed on the O_2 plasma-treated RDRE array in CV measurements. By controlling pore density in the RDRE array, the electrochemical signal gain of the device performance can be optimized. Maximum amplification factor was obtained on high-density RDRE arrays. We envision that this approach will provide an attractive applications combined with ultrasmall volume and efficient trapping of optical field in the zero-dimensional nanopores for spectroelectrochemical investigations. In this context, the use of a dual-ring, instead of a ring-disk, structure is important in that it allows optical access to the cycling redox species.

ASSOCIATED CONTENT

Supporting Information

The Supporting Information is available free of charge on the ACS Publications website at DOI: 10.1021/acs.jpcc.6b01287.

Detailed descriptions of finite-element simulations of electrochemical behavior. (PDF)

AUTHOR INFORMATION

Corresponding Author

*E-mail: pbohn@nd.edu. Tel: +1 574 631 1849. Fax: +1 574 631 8366.

Notes

The authors declare no competing financial interest.

ACKNOWLEDGMENTS

This work was supported by the National Science Foundation grant 1404744 (L.P.Z. and K.F.) and the Defense Advanced Research Projects Agency FA8650-15-C-7546 (D.H.). We gratefully acknowledge Chaoxiong Ma for valuable discussions. Fabrication and structural characterization of the devices studied here were accomplished at the Notre Dame Nanofabrication Facility and the Notre Dame Integrated Imaging Facility, respectively. Their generous support is gratefully acknowledged.

REFERENCES

(1) Kätelhön, E.; Krause, K. J.; Singh, P. S.; Lemay, S. G.; Wolfrum, B. Noise Characteristics of Nanoscaled Redox-Cycling Sensors: Investigations Based on Random Walks. *J. Am. Chem. Soc.* **2013**, *135*, 8874−8881.

(2) Anderson, L. B.; Reilley, C. N. Thin-Layer Electrochemistry: Steady-State Methods of Studying Rate Processes. *J. Electroanal. Chem.* **1965**, *10*, 295−305.

(3) Fan, F.-R. F.; Bard, A. J. Electrochemical Detection of Single Molecules. *Science* **1995**, *267*, 871−874.

(4) Sun, P.; Mirkin, M. V. Electrochemistry of Individual Molecules in Zeptoliter Volumes. *J. Am. Chem. Soc.* **2008**, *130*, 8241−8250.

(5) Singh, P. S.; Katelhon, E.; Mathwig, K.; Wolfrum, B.; Lemay, S. G. Stochasticity in Single-Molecule Nanoelectrochemistry: Origins, Consequences, and Solutions. *ACS Nano* **2012**, *6*, 9662−9671.

(6) Dam, V. A. T.; Olthuis, W.; van den Berg, A. Redox Cycling with Facing Interdigitated Array Electrodes as a Method for Selective Detection of Redox Species. *Analyst* **2007**, *132*, 365−370.

(7) French, R. W.; Gordeev, S. N.; Raithby, P. R.; Marken, F. Paired Gold Junction Electrodes with Submicrometer Gap. *J. Electroanal. Chem.* **2009**, *632*, 206−210.

(8) Amatore, C.; Sella, C.; Thouin, L. Electrochemical Time-of-Flight Responses at Double-Band Generator-Collector Devices under Pulsed Conditions. *J. Electroanal. Chem.* **2006**, *593*, 194−202.

(9) Mampallil, D.; Mathwig, K.; Kang, S.; Lemay, S. G. Redox Couples with Unequal Diffusion Coefficients: Effect on Redox Cycling. *Anal. Chem.* **2013**, *85*, 6053−6058.

(10) French, R. W.; Collins, A. M.; Marken, F. Growth and Application of Paired Gold Electrode Junctions: Evidence for Nitrosonium Phosphate During Nitric Oxide Oxidation. *Electroanalysis* **2008**, *20*, 2403−2409.

(11) Menshykau, D.; Cortina-Puig, M.; del Campo, F. J.; Muñoz, F. X.; Compton, R. G. Plane-Recessed Disk Electrodes and Their Arrays in Transient Generator-Collector Mode: The Measurement of the Rate of the Chemical Reaction of Electrochemically Generated Species. *J. Electroanal. Chem.* **2010**, *648*, 28−35.

(12) Bard, A. J.; Fan, F.-R. F.; Kwak, J.; Lev, O. Scanning Electrochemical Microscopy - Introduction and Principles. *Anal. Chem.* **1989**, *61*, 132−138.

(13) Takahashi, Y.; Shevchuk, A. I.; Novak, P.; Babakinejad, B.; Macpherson, J.; Unwin, P. R.; Shiku, H.; Gorelik, J.; Klenerman, D.; Korchev, Y. E.; Matsue, T. Topographical and Electrochemical Nanoscale Imaging of Living Cells Using Voltage-Switching Mode Scanning Electrochemical Microscopy. *Proc. Natl. Acad. Sci. U. S. A.* **2012**, *109*, 11540−11545.

(14) Batchelor-McAuley, C.; Dickinson, E. J. F.; Rees, N. V.; Toghill, K. E.; Compton, R. G. New Electrochemical Methods. *Anal. Chem.* **2012**, *84*, 669−684.

(15) Han, D.; Kim, Y.-R.; Kang, C. M.; Chung, T. D. Electrochemical Signal Amplification for Immunosensor Based on 3D Interdigitated Array Electrodes. *Anal. Chem.* **2014**, *86*, 5991−5998.

(16) Niwa, O.; Morita, M.; Tabei, H. Electrochemical-Behavior of Reversible Redox Species at Interdigitated Array Electrodes with Different Geometries - Consideration of Redox Cycling and Collection Efficiency. *Anal. Chem.* **1990**, *62*, 447−452.

(17) Ueno, K.; Hayashida, M.; Ye, J. Y.; Misawa, H. Fabrication and Electrochemical Characterization of Interdigitated Nanoelectrode Arrays. *Electrochem. Commun.* **2005**, *7*, 161−165.

(18) Thomas, J. H.; Kim, S. K.; Hesketh, P. J.; Halsall, H. B.; Heineman, W. R. Microbead-Based Electrochemical Immunoassay with Interdigitated Array Electrodes. *Anal. Biochem.* **2004**, *328*, 113−122.

DOI: 10.1021/acs.jpcc.6b01287
J. Phys. Chem. C 2016, 120, 20634−20641

(19) Ito, T.; Maruyama, K.; Sobue, K.; Ohya, S.; Niwa, O.; Suzuki, K. Electrochemical Behavior of Parallel Opposed Dual Electrode in a Microchannel. *Electroanalysis* **2004**, *16*, 2035−2041.
(20) Paixão, T. R. L. C.; Richter, E. M.; Brito-Neto, J. G. A.; Bertotti, M. The Use of a New Twin-Electrode Thin-Layer Cell to the Study of Homogeneous Processes Coupled to Electrode Reactions. *J. Electroanal. Chem.* **2006**, *596*, 101−108.
(21) Han, S.; Zhai, J. F.; Shi, L. H.; Liu, X. Q.; Niu, W. X.; Li, H. J.; Xu, G. B. Rotating Minidisk-Disk Electrodes. *Electrochem. Commun.* **2007**, *9*, 1434−1438.
(22) Vesztergom, S.; Ujvari, M.; Láng, G. G. RRDE Experiments with Potential Scans at the Ring and Disk Electrodes. *Electrochem. Commun.* **2011**, *13*, 378−381.
(23) Yang, T.-H.; Venkatesan, S.; Lien, C. H.; Chang, J. L.; Zen, J. M. Nafion/Lead Oxide-Manganese Oxide Combined Catalyst for Use as a Highly Efficient Alkaline Air Electrode in Zinc-Air Battery. *Electrochim. Acta* **2011**, *56*, 6205−6210.
(24) Henry, C. S.; Fritsch, I. Microfabricated Recessed Microdisk Electrodes: Characterization in Static and Convective Solutions. *Anal. Chem.* **1999**, *71*, 550−556.
(25) Neugebauer, S.; Müller, U.; Lohmüller, T.; Spatz, J. R.; Stelzle, M.; Schuhmann, W. Characterization of Nanopore Electrode Structures as Basis for Amplified Electrochemical Assays. *Electroanalysis* **2006**, *18*, 1929−1936.
(26) Lohmüller, T.; Müller, U.; Breisch, S.; Nisch, W.; Rudorf, R.; Schuhmann, W.; Neugebauer, S.; Kaczor, M.; Linke, S.; Lechner, S.; Spatz, J.; Stelzle, M. Nano-Porous Electrode Systems by Colloidal Lithography for Sensitive Electrochemical Detection: Fabrication Technology and Properties. *J. Micromech. Microeng.* **2008**, *18*, 115011.
(27) Menshykau, D.; O'Mahony, A. M.; del Campo, F. J.; Munõz, F. X.; Compton, R. G. Microarrays of Ring-Recessed Disk Electrodes in Transient Generator-Collector Mode: Theory and Experiment. *Anal. Chem.* **2009**, *81*, 9372−9382.
(28) Li, S.-J.; Li, J.; Wang, K.; Wang, C.; Xu, J.-J.; Chen, H.-Y.; Xia, X.-H.; Huo, Q. A Nanochannel Array-Based Electrochemical Device for Quantitative Label-Free DNA Analysis. *ACS Nano* **2010**, *4*, 6417−6424.
(29) Zhu, F.; Yan, J. W.; Lu, M.; Zhou, Y. L.; Yang, Y.; Mao, B.-W. A Strategy for Selective Detection Based on Interferent Depleting and Redox Cycling Using the Plane-Recessed Microdisk Array Electrodes. *Electrochim. Acta* **2011**, *56*, 8101−8107.
(30) Ma, C.; Contento, N. M.; Gibson, L. R.; Bohn, P. W. Redox Cycling in Nanoscale-Recessed Ring-Disk Electrode Arrays for Enhanced Electrochemical Sensitivity. *ACS Nano* **2013**, *7*, 5483−5490.
(31) Ma, C.; Contento, N. M.; Gibson, L. R.; Bohn, P. W. Recessed Ring-Disk Nanoelectrode Arrays Integrated in Nanofluidic Structures for Selective Electrochemical Detection. *Anal. Chem.* **2013**, *85*, 9882−9888.
(32) Ma, C.; Contento, N. M.; Bohn, P. W. Redox Cycling on Recessed Ring-Disk Nanoelectrode Arrays in the Absence of Supporting Electrolyte. *J. Am. Chem. Soc.* **2014**, *136*, 7225−7228.
(33) Ma, C.; Zaino, L. P., III; Bohn, P. W. Self-Induced Redox Cycling Coupled Luminescence on Nanopore Recessed Disk-Multiscale Bipolar Electrodes. *Chem. Sci.* **2015**, *6*, 3173−3179.
(34) Aguilar, Z. P.; Vandaveer, W. R.; Fritsch, I. Self-Contained Microelectrochemical Immunoassay for Small Volumes Using Mouse IgG as a Model System. *Anal. Chem.* **2002**, *74*, 3321−3329.
(35) Kung, S. C.; van der Veer, W. E.; Yang, F.; Donavan, K. C.; Penner, R. M. 20 μS Photocurrent Response from Lithographically Patterned Nanocrystalline Cadmium Selenide Nanowires. *Nano Lett.* **2010**, *10*, 1481−1485.
(36) Tyagi, P.; Postetter, D.; Saragnese, D. L.; Randall, C. L.; Mirski, M. A.; Gracias, D. H. Patternable Nanowire Sensors for Electrochemical Recording of Dopamine. *Anal. Chem.* **2009**, *81*, 9979−9984.
(37) Valsesia, A.; Lisboa, P.; Colpo, P.; Rossi, F. Fabrication of Polypyrrole-Based Nanoelectrode Arrays by Colloidal Lithography. *Anal. Chem.* **2006**, *78*, 7588−7591.
(38) Lanyon, Y. H.; De Marzi, G.; Watson, Y. E.; Quinn, A. J.; Gleeson, J. P.; Redmond, G.; Arrigan, D. W. M. Fabrication of Nanopore Array Electrodes by Focused Ion Beam Milling. *Anal. Chem.* **2007**, *79*, 3048−3055.
(39) Rauf, S.; Shiddiky, M. J. A.; Trau, M. Drill and Fill" Lithography for Controlled Fabrication of 3D Platinum Electrodes. *Sens. Actuators, B* **2013**, *185*, 543−547.
(40) Dawson, K.; Wahl, A.; Murphy, R.; O'Riordan, A. Electroanalysis at Single Gold Nanowire Electrodes. *J. Phys. Chem. C* **2012**, *116*, 14665−14673.
(41) Kleijn, S. E. F.; Yanson, A. I.; Koper, M. T. M. Electrochemical Characterization of Nano-Sized Gold Electrodes Fabricated by Nano-Lithography. *J. Electroanal. Chem.* **2012**, *666*, 19−24.
(42) von Stackelberg, M.; Pilgram, M.; Toome, V. Bestimmung von Diffusionskoeffizienten einiger Ionen in wäßriger Lösung in Gegenwart von Fremdelektrolyten. I. *Z. Elecktrochem.* **1953**, *57*, 342−350.
(43) Jin, B. K.; Qian, W. J.; Zhang, Z. X.; Shi, H. S. Application of the Finite Analytic Numerical Method 0.1. Diffusion Problems on Coplanar and Elevated Interdigitated Microarray Band Electrodes. *J. Electroanal. Chem.* **1996**, *411*, 29−36.
(44) Zaino, L. P.; Grismer, D. A.; Han, D.; Crouch, G. M.; Bohn, P. W. Single Occupancy Spectroelectrochemistry of Freely Diffusing Flavin Mononucleotide in Zero-Dimensional Nanophotonic Structures. *Faraday Discuss.* **2015**, *184*, 101−115.
(45) Horiuchi, T.; Niwa, O.; Morita, M.; Tabei, H. Limiting Current Enhancement by Self-Induced Redox Cycling on a Micro-Macro Twin Electrode. *J. Electrochem. Soc.* **1991**, *139*, 3549−3553.
(46) Zhu, F.; Yan, J. W.; Pang, S. W.; Zhou, Y. L.; Mao, B. W.; Oleinick, A.; Svir, I.; Amatore, C. Strategy for Increasing the Electrode Density of Microelectrode Arrays by Utilizing Bipolar Behavior of a Metallic Film. *Anal. Chem.* **2014**, *86*, 3138−3145.
(47) Wolfrum, B.; Zevenbergen, M.; Lemay, S. Nanofluidic Redox Cycling Amplification for the Selective Detection of Catechol. *Anal. Chem.* **2008**, *80*, 972−977.

DOI: 10.1021/acs.jpcc.6b01287
J. Phys. Chem. C 2016, 120, 20634−20641